Electronic Confinement and Coherence in Patterned Epitaxial Graphene

Claire Berger,[1,2] Zhimin Song,[1] Xuebin Li,[1] Xiaosong Wu,[1] Nate Brown,[1] Cécile Naud,[2] Didier Mayou,[2] Tianbo Li,[1] Joanna Hass,[1] Alexei N. Marchenkov,[1] Edward H. Conrad,[1] Phillip N. First,[1] Walt A. de Heer*

Ultrathin epitaxial graphite was grown on single-crystal silicon carbide by vacuum graphitization. The material can be patterned using standard nanolithography methods. The transport properties, which are closely related to those of carbon nanotubes, are dominated by the single epitaxial graphene layer at the silicon carbide interface and reveal the Dirac nature of the charge carriers. Patterned structures show quantum confinement of electrons and phase coherence lengths beyond 1 micrometer at 4 kelvin, with mobilities exceeding 2.5 square meters per volt-second. All-graphene electronically coherent devices and device architectures are envisaged.

The fundamental limitations of silicon-based microelectronics have inspired searches for new processes, methods, and materials. We show here that the properties of epitaxial graphene are suitable for coherent nanoscale electronics applications (1). In particular, an ultrathin graphite layer grown on a commercial single-crystal silicon carbide by thermal decomposition has high structural integrity. The single graphene layer at the graphite-SiC interface has impressive two-dimensional (2D) electron gas properties, including long phase coherence lengths (even at relatively high temperatures) and elastic scattering lengths that are determined primarily by the micrometer-scale sample geometry. Magnetotransport measurements of patterned structures reveal signatures of quantum confinement, thus demonstrating that graphene ribbons act as electron waveguides. The material can be patterned, and intricate submicrometer structures can be constructed using standard microelectronics lithography methods, in contrast to the closely related carbon nanotube electronics. The transport properties show that electrons in the interfacial graphene layer dominate the transport and that they are Dirac fermions, as recently observed in mechanically exfoliated graphene layers (2, 3). The properties of Dirac fermions, which are also responsible for transport in carbon nanotubes (4), can be conveniently explored in epitaxial graphene.

The electronic properties of sp²-bonded carbon structures (which include bulk graphite, graphene ribbons, carbon nanotubes, and aromatic molecules) result from the overlap of p_z atomic orbitals on neighboring carbon atoms. Simple tight-binding calculations show that in graphene, π-bands are formed, with electronic energy dispersion $E(p) = \pm v_0 |p|$, where the carrier momentum $p = \hbar\sqrt{(k_x^2 + k_y^2)}$ (5–7), v_0 is the velocity, and $\hbar$ is Planck's constant divided by 2π. Consequently, like photons, the velocity of electrons is independent of energy. The predicted velocity $v_0 = 3a_0\gamma_0/2\hbar \approx 10^6$ m/s, where $\gamma_0 \sim 3$ eV is the interatomic overlap energy and $a_0 = 1.42$ Å is the interatomic spacing. The Fermi surface of neutral graphene (Fermi energy $E_F = 0$) shrinks to a point, so that it is a zero-band-gap semiconductor (6). When carriers in graphene are confined, their properties depend on the confinement geometry, as is true for other 2D electron gases (8). However, in contrast to conventional 2D electron systems, which are electrostatically confined at a buried interface, epitaxial graphene (1, 9, 10) is a well-defined material that is robust, so that in principle it can be sculpted down to the molecular level.

We present production methods for epitaxial graphene (EG) and show that the transport properties of a representative patterned EG structure are due to carrier confinement and coherence. From magnetoresistance (MR) and Hall-effect measurements, we find that the material that dominates the transport is in fact graphene. This conclusion follows from the following measured properties: Berry's phase $\Phi_B = \pi$, Fermi temperature $T_F = 2490$ K, Fermi velocity $v_0 = 1.0 \times 10^6$ m/s, mobility

Fig. 1. Production and characterization of EG. (**A**) LEED pattern (71 eV) of three monolayers of EG on 4H-SiC(000$\bar{1}$) (C-terminated face). The outermost hexagon (spots aligned on the vertical) is graphene 1 × 1 diffraction. Bright sixfold spots aligned on the horizontal are SiC 1 × 1. The smallest hexagon is the result of a $\sqrt{3} \times \sqrt{3}$ reconstruction of the interfacial layer, as are the spots lying just inside the graphene pattern. Graphene thickness is determined via Auger spectroscopy (attenuation of Si peaks). (**B**) AFM image of graphitized 4H-SiC, showing extended terraces. STM studies indicate that the graphite is continuous over the steps (1). (**C**) STM image of one monolayer of EG on SiC(0001). Tunneling conditions (tip bias −0.8 V, current 100 pA) preferentially image structure beneath the graphene layer. Two interface corruga-

tions are apparent, with periods 6 × 6 (1.8-nm triangular superlattice) and $\sqrt{3} \times \sqrt{3}$ (smaller spots with 0.54-nm spacing) relative to the SiC surface unit cell. (**D**) STM image of interface reconstruction beneath one monolayer of graphene on SiC(0001) obtained after lithography. General features are as seen in (C). (**E**) SEM of patterned EG. Dark regions are the EG (still coated with electron-beam resist). (**F**) EFM of another patterned EG sample, showing a horizontal ribbon (bright contrast) with tapered voltage contacts left and right, which is flanked by diagonally oriented side gates above and below the ribbon. Contrast is obtained through electrostatic forces between the probe and the graphene structure to which potentials are applied, thus allowing functioning devices to be measured.
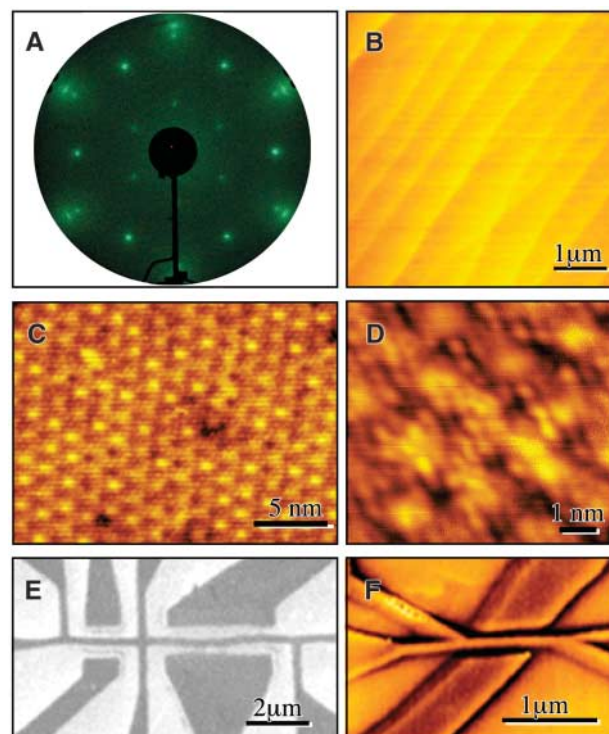
[1]School of Physics, Georgia Institute of Technology, Atlanta, GA 30332, USA. [2]Laboratoire d'Études des Propriétés Électroniques des Solides, CNRS, BP166, 38042 Grenoble Cedex 9, France.

*To whom correspondence should be addressed. E-mail: walt.deheer@physics.gatech.edu

$\mu = 2.7$ m²/V·s, carrier diffusion constant $D = 0.3$ m²/s, elastic mean free path $l_s = 600$ nm, and phase coherence lengths of $l_\phi = 1.1$ μm at 4 K and 500 nm at 58 K. Furthermore, quantum-confined states are observed.

The production of EG on diced (3 mm by 4 mm) commercial SiC wafers (11) is illustrated in Fig. 1. In summary, the steps are (i) hydrogen etching to produce atomically flat surfaces (12), (ii) vacuum graphitization to produce an ultrathin epitaxial graphite layer (9, 10), (iii) application of metal contacts (Pd, Au), (iv) electron-beam patterning and development, (v) oxygen plasma etch to define graphite structures, and (vi) wire bonding. To date, more than 200 SiC sample blanks have been processed, of which 22 have been patterned and measured in detail [see also (1)]. The structural order has been characterized by low-energy electron diffraction (LEED), Auger electron spectroscopy, x-ray diffraction (13), and scanning tunneling microscopy (STM) (1). The electronic structure has been characterized by angle-resolved photoelectron spectroscopy [ARPES (14)], scanning tunneling spectroscopy (STS) (1), and electronic transport [see below and (1)]. Patterned surfaces are routinely measured by atomic force microscopy (AFM) and electrostatic force microscopy (EFM) under ambient conditions. The results are summarized in Fig. 1. As evident from LEED, an ultrathin graphite layer grows epitaxially on the SiC(000$\bar{1}$) surface. X-ray diffraction shows that graphene grown on the 000$\bar{1}$ face has a structural coherence of at least 90 nm (13). On the Si-terminated SiC(0001) surface, LEED and STM measurements reveal a $(6\sqrt{3} \times 6\sqrt{3})$R30° interface reconstruction. STS measurements reveal the graphitic band structure, and STM and STS together suggest that graphene layers can remain continuous over steps on the SiC surface (1). The ARPES data (for two EG layers on 0001 SiC) suggest a Dirac electronic dispersion and a Fermi temperature of 2700 K (14). This relatively large energy indicates that the interface layer is charged, with a charge density $\sigma \sim 1 \times 10^{12}$ electrons/cm² (see below). As usual for such interfaces, the electric field caused by the surface charge compensates the work function difference between the materials. Only the interface layer is expected to be highly charged (15, 16); the (few) other layers are essentially neutral. Thus, the interface layer should dominate the transport properties, which are essentially identical to those of isolated graphene (see below). The interface layer is further distinguished from any others by a weak superlattice structure imposed by the epitaxial match to SiC (1).

We briefly summarize some relevant properties of confined Dirac electrons in graphene. For a graphene ribbon of width W, the boundaries impose a constraint on the transverse motion so that (for not too small n) k_y is quantized: $k_y = n\pi/W$, where n is an integer (17). Hence, the energy of the nth electronic subband is $E_n(p_x) = v_0|p| = \hbar v_0 \sqrt{(k_x^2 + k_y^2)} = \sqrt{(E_x^2 + n^2 \Delta E^2)}$, where $\Delta E = \Delta E(W) = \pi \hbar v_0 / W \sim (2 \text{ eV·nm})/W$, and $E_x = \hbar v_0 k_x$. Hence, these electrons propagate like electromagnetic waves in waveguides. A more detailed analysis shows that undoped graphene (i.e., $E_F = 0$) can be tuned to be either a metal or a semiconductor with a band gap on the order of $\Delta E(W)$ (18, 19). This is an important property that undoped graphene ribbons share with undoped carbon nanotubes.

For any 2D electron system (20–22), a perpendicular magnetic field B creates a discrete energy spectrum (Landau levels) due to quantization of the cyclotron orbits (radius $R_c = p/eB$). The energy states for Dirac electrons are given by $E_n(B) = \sqrt{(2neBv_0^2\hbar)}$ (2, 3, 23) where n is the integer Landau level index [by contrast, $E_n^*(B) = (n + \frac{1}{2})\hbar eB/m^*$ for "normal" electrons, where m^* is the effective mass (20)]. Shubnikov–de Haas (SdH) MR maxima were observed at magnetic fields B_n such that $E_n(B_n) = E_F$. Hence, $B_n = B_0/n$, where $B_0 = E_F^2/(2ev_0^2\hbar) = \hbar k_F^2/2e$ (24–26).
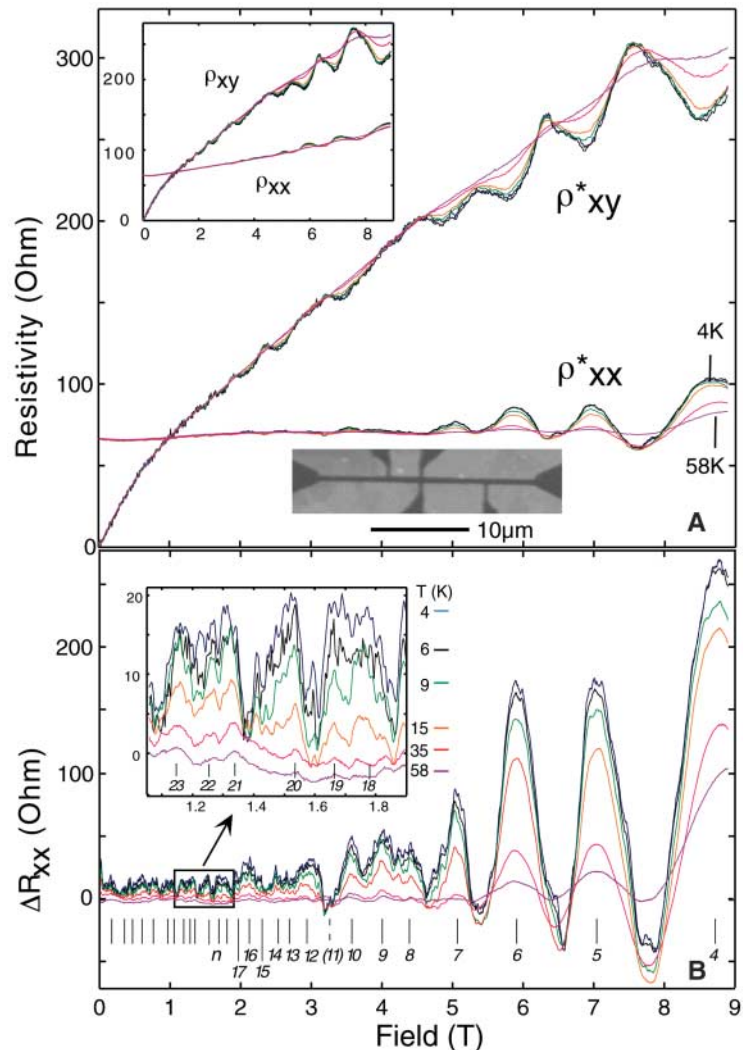

Fig. 2. Magnetotransport of a lithographically patterned graphene Hall bar (SEM micrograph, lower inset) measured at temperatures $T = 4, 6, 9, 15, 35,$ and 58 K, and magnetic fields -9 T $\leq B \leq 9$ T. (**A**) Components of the resistivity tensor ρ are shown (inset; $\rho_{xx} = R_{xx}W^*/L$, $\rho_{xy} = R_{xy}$). ρ^* is derived from ρ: $(\rho^*)^{-1} = \rho^{-1} - (\rho^0)^{-1}$, where $\rho_{xx}^0 = 1125$ ohms and $\rho_{xy}^0 = 0$. Hence, the slight slope in ρ_{xx} appears to be caused by a conducting layer ρ^0 on top of the graphene layer. The graphene mobility is $\mu^* = 2.7$ m²/V·s. (**B**) ΔR_{xx} obtained from the measured R_{xx} by subtracting a smooth background. Peak positions are indicated (peak 11 is missing). The peak character changes near $B = 4.5$ T. The peak amplitudes are essentially constant below 2 T and increase above 2 T. Inset: Detail of the oscillations near $B = 1$ T. The amplitude of the universal conductance fluctuations (noise-like structures) increases with decreasing temperature.

Next, consider a graphene ribbon of width W in a magnetic field. It is intuitively clear that for low magnetic fields, when $W < 2R_c$ the ribbon cannot support a cyclotron orbit, so the above picture needs to be modified (20, 22). For graphene, $2R_c = 4n/k_F$, which is 260 nm for $n = 20$. Quantitatively, Berggren et al. (27) found that for a normal 2D electron system confined to a strip of width W, $E_n(B,W) \approx \sqrt{[E_n(W)^2 + E_n(B)^2]}$, where $E_n(W) = (n\pi\hbar/W)^2/2m^*$ (20). Analogously, for graphene

ribbons, $E_n(W) = n\pi\hbar v_0/W$, and an approximate expression for the energy levels can be obtained (28):

$$E_n(B,W) \approx [E_n(W)^4 + E_n(B)^4]^{1/4} =$$
$$\{[n\pi\hbar v_0/W]^4 + [2neBv_0^2\hbar]^2\}^{1/4} \quad (1)$$

Recent numerical results agree very well with this analytical form (29). As for normal electrons, SdH peaks are expected when $E_n(B_n,W) =$ E_F. Consequently $B_n = B_0/n$ for small n, whereas for large $n \sim n_{max}$ the peak spacing becomes more regular: $B_n - B_{n+1} \sim B_0/n_{max}$, where $n_{max} = E_F/\Delta E(W)$ is the number of populated transverse modes.

To illustrate the properties of carrier confinement and coherence, we next present magneto-transport data from a representative patterned EG structure. The sample is a Hall bar (ribbon) of width $W = 500$ nm created on the graphitized $000\bar{1}$ face of a high-quality semi-insulating 4H-SiC substrate (Fig. 2A, lower inset). Contacts are bonded on Pd/Au deposited pads. Four-point measurements were made using standard lock-in methods, with excitation currents through the ribbon limited to 100 nA. Voltages were measured over a 6-μm length L of the ribbon. MR and Hall-effect data were acquired at six temperatures from 4 to 58 K and in magnetic fields from −9 to +9 T. Field sweeps were repeated to verify reproducibility.

Figure 2A shows that $\rho_{xx} = R_{xx} W^*/L$ (where ρ_{xx} is the resistivity and W^* the effective ribbon width), and the Hall resistance $R_{xy} = \rho_{xy}$ of the sample. ρ_{xx} increases approximately linearly with increasing field. At high fields, SdH oscillations are clearly seen in the ρ_{xx} curves and step-like features are observed in ρ_{xy}. Subtracting a common smooth curve from the MR data reveals a rich, reproducible, and temperature-dependent structure (Fig. 2B). Pronounced, regularly spaced SdH maxima are distinguished clearly at high fields, whereas at low fields MR peaks are visible but are less well defined. Increasing the temperature decreases the amplitude of the peaks, with the high-field peaks decreasing more slowly than the low-field peaks. At a given temperature the amplitudes are relatively constant for $B < 2$ T and increase uniformly for $B > 2$ T. Positions of 29 distinct SdH peaks B_n have been identified and are indicated in Fig. 2B. Features are identified as SdH peaks when they present a clear maximum, and they are present at all of the measured temperatures. A complication is the reproducible fine structure observed throughout the MR spectra, which can obscure the SdH peaks for small fields. These are (universal) conductance fluctuations. As discussed below, the temperature dependences of universal conductance fluctuations (UCFs) and SdH oscillations are well understood and quite distinct. Incorporating this information results in an ambiguity of less than 10% in the number of peaks assigned according to the above criteria.

A Landau plot of the peaks [i.e., B_n^{-1} versus n (20, 24, 30)] is shown in the inset of Fig. 3B. The low index peaks ($n = 4$ to 12) define a straight line: $B_n^{-1} = (n + \gamma)B_0^{-1}$ with $B_0 = 35.1 \pm 0.8$ T and $\gamma = -0.05 \pm 0.14$. This value of γ is consistent with a Berry phase $\Phi_B = \pi$, as expected for Dirac fermions and previously observed in graphene (2, 3, 23, 26). It is specifically not consistent with $\gamma = \pm 0.5$, as would
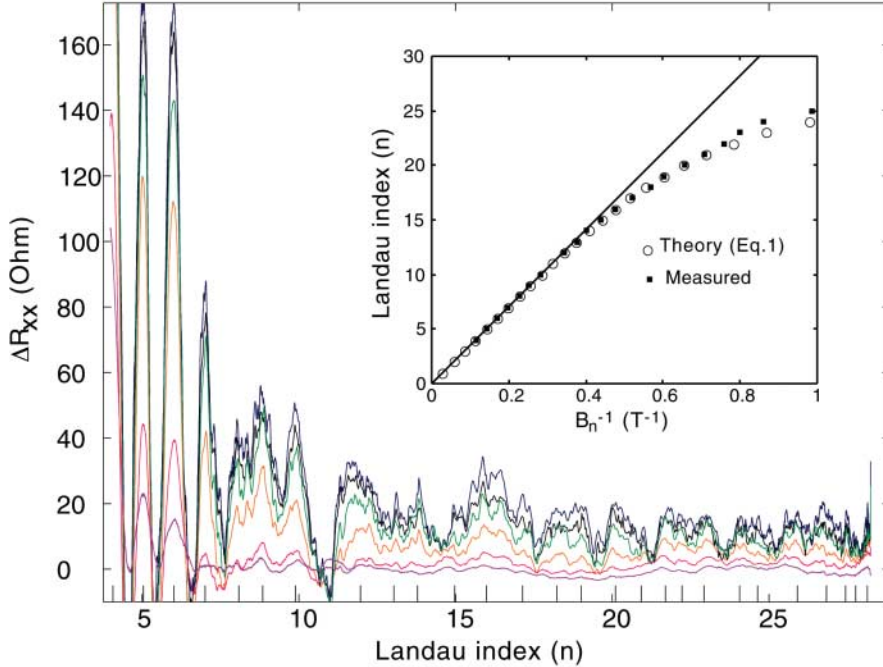

Fig. 3. Demonstration of confinement. Inset: Landau plot demonstrating the linear dependence of the measured inverse MR peak positions $1/B_n$ on the peak index n when the cyclotron diameter is smaller than the ribbon width. The linear fit for small n (bold line) intercepts the ordinate at $n = 0.05$, consistent with the graphene value $\gamma = 0$ and Berry's phase $\Phi_B = \pi$ (the slope of the fit corresponds to B_0, which determines k_F). The observed deviations from linearity occur for larger n when confinement becomes important; these correspond well with Eq. 1 predictions. The confinement is further illustrated by plotting ΔR_{xx} in terms of the variable $n(B)$ from Eq. 1, which shows that the peak positions approximately coincide with integers. For color code, see Fig. 2.

Fig. 4. Landau level excitation energies $\Delta E(B)$. Inset: Normalized MR amplitudes $\Delta R_{xx}(B,T)/\Delta R_{xx}(B,T = 4$ K) are fitted to Eq. 2; fit examples are shown for $B =$ 7 T ($n = 5$), 5 T ($n = 7$), and 1 T ($n = 23$–24). Note that $\Delta E(B)$ increases approximately linearly for $B > 2$ as predicted theoretically (open circles from Eq. 1). In this region $\Delta E(B_n) \sim E_F/2n$. For smaller fields $\Delta E(B_n) \rightarrow E_F/n_{max}$, where n_{max} is the number of subbands in zero field. Good correspondence with theory is found for $W^* = 270$ nm.
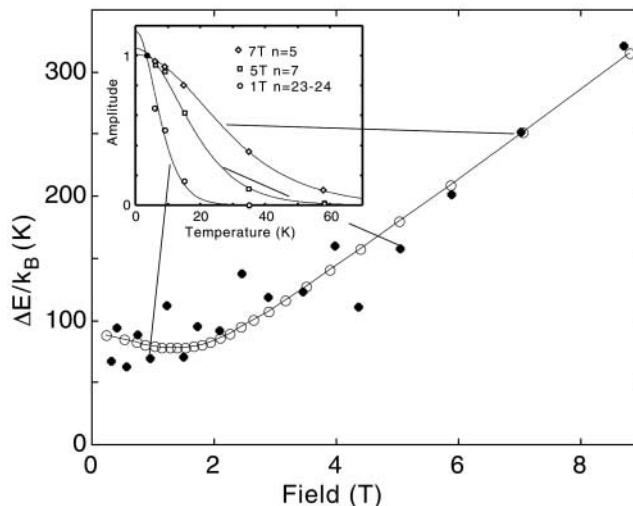
be the case for normal electrons (23). Note that the same result was found for various subsets of peaks in the interval $n = 4$ to 12. For a 2D electron gas in general, we have $k_F = \sqrt{(2eB_0/\hbar)}$. From B_0 we find $k_F = 3.3 \times 10^8$/m, and the carrier density $n_s = g_s g_v k_F^2/4\pi = 3.4 \times 10^{16}$ electrons/m² (where $g_s = 2$ and $g_v = 2$ are the spin and valley degeneracies) (20, 21). The deviation from linearity for the larger index peaks ($n > 14$; $B < 2.5$ T; $2R_c > 170$ nm) indicates confinement (20, 27), as explained below.

We next analyze the individual SdH peaks. The amplitudes of SdH peaks decrease with increasing temperature because higher Landau levels are thermally populated. The temperature dependence of the peak amplitudes is given by the Lifshitz-Kosevich (LK) equation (23, 31):

$$A_n(T)/A_n(0) = u/\sinh(u) \qquad (2)$$

where $A_n(T)$ is the peak amplitude (or peak area) of the nth SdH peak at temperature T, and $u = 2\pi^2 k_B T/\Delta E(B)$, where $\Delta E(B) = E_{n+1}(B) - E_n(B)$. Experimental values for $\Delta E(B)$ were determined by fitting SdH peaks to the LK equation for six different temperatures. In Fig. 4 the results are plotted as solid circles; values of $\Delta E(B)$ calculated from Eq. 1 are shown as open circles. A nearly linear increase for $B > 4$ T and saturation at low fields is observed in both theory and experiment. For large B, $\Delta E(B) \sim E_F B/2B_0 = E_F/2n$; for small B, $\Delta E(B) = \hbar\pi v_0/W$. Consequently, the data in Fig. 4 can be used to find $E_F/k_B = 2490 \pm 80$ K and $v_0 = E_F/\hbar k_F = E_F/\hbar\sqrt{(2eB_0/\hbar)} = (1.00 \pm 0.03) \times 10^6$ m/s. Our experimental v_0 agrees remarkably well with the accepted value for graphene (6). Furthermore, E_F is also consistent with recent ARPES measurements (14) on two-layer EG grown on SiC(0001), which found $E_F/k_B = 2700$ K. Hence, experimental evidence (measured Φ_B, v_0, E_F) strongly supports the conclusion that the material is indeed graphene.

For small B, the saturation of $\Delta E_n(B)/k_B$ at 80 ± 10 K indicates quantum confinement. The number of confined subbands should be $n_{max} \sim E_F/\Delta E(B \to 0) = 31 \pm 3$, consistent with the observed $n_{max} = 29 \pm 3$. However the hard wall boundary condition would predict that $n_{max} = Wk_F/\pi = 52$. This discrepancy suggests that the carrier confinement width of the ribbon is less than the lithographic width $W = 500$ nm (subsequent AFM and EFM studies confirmed that the physical width of the ribbon is compatible with the lithographic width; this does not preclude edge roughness effects). In fact, the best fit to the data using Eq. 1 is for $W^* = 270$ nm, as shown in Fig. 4 (see below for further evidence of reduced width). Similar discrepancies have been observed in several ribbons. The smaller effective width may be

related to carrier scattering from steps on the substrate (Fig. 1; steps tend to run parallel to the ribbon) or to a stronger confinement potential caused by charge transfer to states at the ribbon edges (edge roughness, chemisorbed molecules, and intrinsic edge states could contribute), or it may have a more fundamental origin. In Fig. 3 the MR data are presented with the Landau index $n(B)$ as the abscissa, obtained by inversion of Eq. 1 (for $E_n = E_F$), where the experimental values $v_0 = 1.0 \times 10^6$ m/s, $E_F = 2490$ k_B, and $W^* = 270$ nm were used. If Eq. 1 is correct, the measured SdH peaks should coincide with integers. The correspondences up to $n = 22$ are remarkable (note that the $n = 11$ peak is missing at low T), providing additional support for our conclusion that the SdH peaks are determined by both Landau orbital quantization and transverse quantum confinement.

The overall linear increase in the MR (Fig. 1A, inset) may result from a conducting layer on top of the graphene [i.e., a thin graphite layer, consistent with independent x-ray measurements on similar samples (13)]. The slope is removed completely by subtracting from the measurement the conductivity of a layer with resistivity $\rho^0_{xx} = 1125$ ohms/square, and with negligible Hall coefficient. This procedure results in ρ^*_{xx} and ρ^*_{xy} values that are similar to those reported for isolated graphene. Hence, the resistivity of the

graphene layer is $\rho^*_{xx} = 68$ ohms/square, versus 63 ohms/square for the sample before correction. The integrated carrier density derived from the Hall resistance is $n_{Hall} = 6.5 \times 10^{16}$/m², compared with $n_s = 3.4 \times 10^{16}$/m² found for the graphene layer (see above). The difference can be attributed to the integrated carrier density of the conducting (presumably neutral graphite) layer. Hence, we find the graphene mobility $\mu^* = (n_s e\rho^*)^{-1} = 2.7$ m²/V·s, and carrier diffusion constant $D = E_F/2n_s e^2\rho^* = 0.30$ m²/s. From $D = l^* v_0/2$, we obtain $l^* = 600$ nm, where l^* is the carrier mean free path in the graphene. This value is in excellent agreement with the limiting value $l^* \sim 3\pi W^*/4 = 635$ nm for a ribbon 270 nm wide with only diffuse elastic boundary scattering (20), which implies that the resistance is determined primarily by the confining geometry and not by defect scattering in the material.

Alternatively, the conductance of a graphene ribbon can be estimated from the Landauer equation (21): $G = (e^2/h)g_s g_v \Sigma T_n$, where ΣT_n is the sum over transmission coefficients of the nth modes ($0 \leq T \leq 1$). The T_n values are obtained approximately as $T_n = l_n/L$, where l_n is the mean free path of the nth mode (21). If we assume elastic scattering at the boundaries without mode mixing, then l_n is the distance along the wire between scattering events for the nth mode— that is, $l_n = k_x/k_n W = W[(k_F W/n\pi)^2 - 1]^{1/2}$. Hence, $G = (e^2/h)(g_s g_v W^*/L) \Sigma[(n_{max}/n)^2 - 1]^{1/2}$.
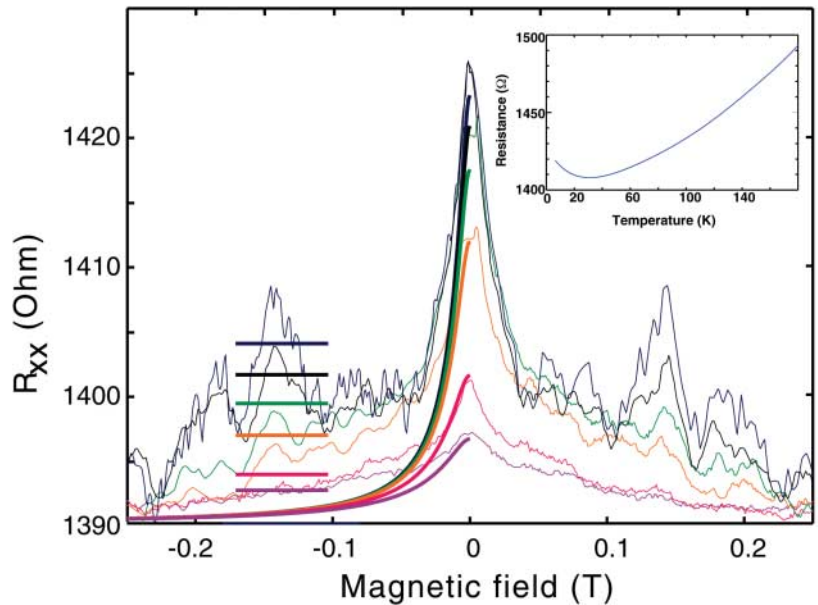

Fig. 5. Electronic coherence determined from weak localization and conductance fluctuations. The weak localization peak observed in the MR near $B = 0$ results from electronic coherent backscattering effects. The temperature dependence of the absolute amplitudes and the widths depend on the phase coherence length $l_\phi(T)$ and the geometry [note the low-temperature saturation of $l_\phi(T) \sim 1.1$ μm]. The UCF structures have widths that are similar to the WL peak (∼0.03 T, considerably narrower than the SdH peaks). The theoretical fits (bold lines, plotted only for $B < 0$), using only $l_\phi(T)$ as a parameter, describe reasonably well both the WL peaks and the UCF amplitudes (bold horizontal lines). Inset: Sample resistance as a function of temperature for $B = 0$.

With $W^* = 270$ nm, $L = 6$ μm, and $n_{max} = 29$, we find $R = 1/G = 1430$ ohms, or $\rho_g = RW^*/L = 64$ ohms/square, in remarkable agreement with experiment.

The sample resistance decreased uniformly from 1490 ohms at $T = 180$ K to a minimum of 1410 ohms at $T = 30$ K, below which it increased (Fig. 5, inset). From 300 to 30 K, the resistance decreased only 13%, which indicates [from Matthiessen's rule (20, 21)] that the electron phonon-scattering time is $\sim 4 \times 10^{-12}$ s at 300 K. The increase of resistance below 30 K is caused by the increasing phase coherence length l_ϕ (20, 22, 32). The resistance increase is a manifestation of constructive quantum interference between time-reversed trajectories, which enhances the probability for an electron to be localized at a scattering site (20, 22, 32). This well-understood weak localization (WL) effect is undone in a magnetic field because time reversal symmetry is lifted (20, 22). The pronounced peak in the low-field MR at $B = 0$ shows this WL effect (Fig. 5). Clear universal conductance fluctuations flank the peak. The reproducible UCFs are caused by quantum interference from elastic scatterers (e.g., at the ribbon edges). For all fields, the widths of UCF features are similar to the WL peak width, in contrast to the SdH peaks, which are much wider. The WL peak saturates at low temperatures (peaks for 4, 6, and 9 K are similar), whereas the amplitude of the UCFs increases very rapidly with decreasing temperature (which also distinguishes UCFs from SdH peaks).

Weak localization and UCFs have been exhaustively investigated in 2D electron systems. Before saturation below 9 K, the observed decrease of the WL peak with increasing T fits a $T^{-2/3}$ dependence, which indicates that electron-electron scattering is the primary dephasing mechanism (22). The decrease in amplitude of the UCFs with increasing T is caused by a reduction of l_ϕ combined with "thermal smearing," which is characterized by the thermal length $l_T = \sqrt{(\hbar D/k_B T)}$.

On the other hand, the WL is not sensitive to l_T. Its width ΔB is essentially determined by the field for which an electron trajectory of length l_ϕ encloses one flux quantum (for this sample $l_\phi \gg W$, so that flux cancellation effects also need to be taken into account). Following the thorough development reviewed by Beenakker and van Houten (20), the field is parameterized in terms of $l_B = \sqrt{D\tau_B}$, where $\tau_B = 3l_m^2 l^*/(W^2 v_0)(4\pi l_m^2/3 W l^* + 1)$, and $l_m = (\hbar/eB)^{1/2}$ is the magnetic length. The WL contribution to the conductance (for $l_\phi \gg l^* \gg W$) is

$$\Delta G_{WL} = -4(G_0/L)[(l_\phi^{-2} + l_B^{-2})^{-1/2} - (l_\phi^{-2} + l_B^{-2} + l^{*-2})^{-1/2}] \quad (3)$$

and the root mean square amplitude of the UCFs is given by

$$\Delta G_{UCF} = \sqrt{24} G_0 (l_\phi/L)^{3/2}[1 + (9/2\pi)(l_\phi/l_T)^2]^{-1/2} \quad (4)$$

The only free parameter in these expressions is $l_\phi(T)$. The origin of the commonly observed low-temperature saturation of the WL is still debated intensely (22). Here we assume that it is caused by a physical limitation to l_ϕ, which appears to be the finite sample length. The effective phase coherence length $l_\phi^* = [l_\phi(T)^{-2} + (L_{sat}/2\pi)^{-2}]^{-1/2}$ saturates at $L_{sat}/2\pi$ (22). The fits shown in Fig. 5 correspond to $L_{sat} = 7$ μm and $l_\phi(T) = (7 \text{ μm})T^{-2/3}$ [at 4 K, $l_\phi^* = 1.1$ μm, and $\tau_\phi = (l_\phi^*)^2/D = 4 \times 10^{-12}$ s; at 58 K, $l_\phi^* = 430$ nm, and $\tau_\phi = 6 \times 10^{-13}$ s].

This analysis clearly shows that the resistance of the graphene ribbon is determined primarily by boundary scattering, with a coherence length far larger than the effective ribbon width, even at 58 K. Therefore, as also shown in our analysis of SdH oscillations, the low-field resistance depends directly on the eigenmodes of laterally confined carriers in the graphene ribbon. Other samples indicate that the width dependence of resistance can persist up to room temperature. Because electron-phonon scattering is weak even at room temperature (see above), electron-electron scattering should continue to be the dominant dephasing mechanism under ambient conditions (such scattering affects the resistance only through phase-breaking, i.e., by limiting l_ϕ). Accordingly, on the basis of the measurements presented here, we expect to see quantum interference effects over distances exceeding 100 nm at room temperature (and beyond 400 nm at liquid nitrogen temperature). Moreover, quantum confinement should be observable at room temperature in ribbons as wide as 50 nm. In this context, we also note that a ribbon 100 nm wide has been observed to sustain a current of >100 μA at room temperature, and that, like nanotubes (33), the conductance of graphene ribbons increases approximately linearly with bias voltage at high bias.

These results raise new possibilities for coherent EG electronics on an attractive size scale and at relatively high temperatures. The demonstrated material and transport properties of EG could allow electronic devices and interconnects to be designed that rely on the wave properties of electrons and holes, so that interference-based electronic switches can be envisioned. Nanotubes, on the other hand, require metallic interconnects that destroy phase coherence. Furthermore, graphene is an extremely robust material that has the potential to be patterned with atomic precision down to the molecular level. Such precision might be achieved through a combination of standard lithographic and chemical methods, enabling a wide variety of coherently connected molecular structures. Finally, we note that it has been previously determined that the carrier density can be controlled electrostatically (1, 16, 34) and that chemical doping of the edges also is feasible (1, 35). Consequently, epitaxial graphene provides a platform for the science and technology of coherent graphene molecular electronics.

References and Notes

1. C. Berger et al., J. Phys. Chem. B **108**, 19912 (2004).
2. K. S. Novoselov et al., Nature **438**, 197 (2005).
3. Y. B. Zhang, Y. W. Tan, H. L. Stormer, P. Kim, Nature **438**, 201 (2005).
4. T. Ando, T. Nakanishi, R. Saito, J. Phys. Soc. Jpn. **67**, 2857 (1998).
5. P. R. Wallace, Phys. Rev. **71**, 622 (1947).
6. B. T. Kelly, Physics of Graphite (Applied Science, London, 1981).
7. The momentum is with reference to the K point in graphene, i.e., $E = v_0 \hbar |k - k(K)|$, where k is the wave vector.
8. Carbon nanotubes are a specific example of confined graphene, where the momentum perpendicular to the axis is quantized according to $k_{perp} = n/D$, where D is the diameter.
9. I. Forbeaux, J. M. Themlin, J. M. Debever, Phys. Rev. B **58**, 16396 (1998).
10. A. Charrier et al., J. Appl. Phys. **92**, 2479 (2002).
11. Cree Inc., High Purity, R Grade 4H SiC.
12. V. Ramachandran, M. F. Brady, A. R. Smith, R. M. Feenstra, D. W. Greve, J. Electron. Mater. **27**, 308 (1998).
13. J. Hass et al., arxiv.org/abs/cond-mat/0604206 (2006).
14. E. Rollings et al., arxiv.org/abs/cond-mat/0512226 (2005).
15. P. B. Visscher, L. M. Falicov, Phys. Rev. B **3**, 2541 (1971).
16. Y. B. Zhang, J. P. Small, M. E. S. Amori, P. Kim, Phys. Rev. Lett. **94**, 176803 (2005).
17. M. Fujita, K. Wakabayashi, K. Nakada, K. Kusakabe, J. Phys. Soc. Jpn. **65**, 1920 (1996).
18. K. Nakada, M. Fujita, G. Dresselhaus, M. S. Dresselhaus, Phys. Rev. B **54**, 17954 (1996).
19. K. Wakabayashi, Phys. Rev. B **64**, 12 (2001).
20. C. W. J. Beenakker, H. van Houten, Quantum Transport in Semiconductor Nanostructures, vol. 44 (Academic Press, New York, 1991), and reference therein (also available at arxiv.org/abs/cond-mat/0412664).
21. S. Datta, Electronic Transport in Mesoscopic Systems (Cambridge Univ. Press, Cambridge, 1995).
22. J. J. Lin, J. P. Bird, J. Phys. Condens. Matter **14**, R501 (2002).
23. S. G. Sharapov, V. P. Gusynin, H. Beck, Phys. Rev. B **69**, 075104 (2004).
24. D. E. Soule, J. W. McClure, L. B. Smith, Phys. Rev. A. **134**, A453 (1964).
25. D. E. Soule, Phys. Rev. **1**, 708 (1958).
26. I. A. Luk'yanchuk, Y. Kopelevich, Phys. Rev. Lett. **93**, 166402 (2004).
27. K. F. Berggren, G. Roos, H. van Houten, Phys. Rev. B **37**, 10118 (1988).
28. Equation 1 is obtained by applying the interpolation scheme of (27) to Dirac electrons. Applying the Schrödinger equation $H|\Psi\rangle = E|\Psi\rangle$ twice gives $H_{eff}|\Psi\rangle = E_{eff}|\Psi\rangle$ with $H_{eff} = H^2$ and $E_{eff} = E^2$. It can be shown that $H_{eff} = H^2$ describes free-like electrons close to the band edges (either from the Dirac equation or the tight-binding model; the origin of energies is taken at the band edges). Using the square root interpolation formula of (27) applied to $H_{eff} = H^2$ gives $E_n = \sqrt{E_{eff_n}}$ for the energies at the bottom of band n.
29. N. M. R. Peres, A. H. Castro Neto, F. Guinea, arxiv.org/abs/cond-mat/0603771 (2006).
30. We follow the convention of indexing the MR peaks (24, 25) rather than the valleys.
31. I. M. Lifshitz, A. M. Kosevich, Sov. Phys. JETP **2**, 636 (1956).

32. B. L. Altshuler, A. G. Aronov, Eds., *Electron-Electron Inter-actions in Disordered Systems* (Elsevier, Amsterdam, 1985).
33. P. Poncharal, C. Berger, Y. Yi, Z. L. Wang, W. A. de Heer, *J. Phys. Chem. B* **106**, 12104 (2002).
34. K. S. Novoselov *et al.*, *Science* **306**, 666 (2004).
35. N. M. R. Peres, F. Guinea, A. H. Castro Neto, arxiv.org/abs/cond-mat/0512091 (2005).

Imaging Bond Formation Between a Gold Atom and Pentacene on an Insulating Surface

Jascha Repp,[1]* Gerhard Meyer,[1] Sami Paavilainen,[2] Fredrik E. Olsson,[3] Mats Persson[4]

A covalent bond between an individual pentacene molecule and a gold atom was formed by means of single-molecule chemistry inside a scanning tunneling microscope junction. The bond formation is reversible, and different structural isomers can be produced. The single-molecule synthesis was done on ultrathin insulating films that electronically isolated the reactants and products from their environment. Direct imaging of the orbital hybridization upon bond formation provides insight into the energetic shifts and occupation of the molecular resonances.

Electron transport through single molecules in contact with metal electrodes has turned out to depend crucially on the details of the contact geometry (*1*), resulting in poor reproducibility of experiments in different setups. Control on the contact formation will not only have to include the atomic-scale geometry itself, but also coherent (strong coupling) versus incoherent (weak coupling) electron

[1]IBM Zurich Research Laboratory, 8803 Rüschlikon, Switzerland. [2]Institute of Physics, Tampere University of Technology, 33720 Tampere, Finland. [3]Department of Applied Physics, Chalmers, 41296 Göteborg, Sweden. [4]Surface Science Research Centre and Department of Chemistry, The University of Liverpool, Liverpool L69 3BX, UK.

*To whom correspondence should be addressed. E-mail: jre@zurich.ibm.com

transport, coupling with respect to the molecular orbitals, and possibly also the phase of the orbital wave function at the contact point.

We show here that such control can be achieved for connecting metal atoms to π-conjugated molecules on insulating NaCl films by means of single-molecule chemistry (*2–5*) in a scanning tunneling microscope (STM) junction. The atomic precision in STM manipulation and single-molecule chemistry can be exploited to create different kinds of contacts between a gold atom and a pentacene molecule. The gold atom can be brought into various positions a few angstroms away from the molecule, which facilitates an electron tunneling current between the atom and the molecule (weak coupling). Alternatively, the gold atom

can be covalently bound to the pentacene molecule to form a metal-organic complex, which is accompanied by a strong and coherent electronic coupling between the two constituents, as can be deduced from STM images. Moreover, the possibility of creating different structural isomers by bringing together the reactants in different orientations enables control of the phase of the molecular orbital at the contact point. The influence of the contact formation on the electronic structure of the complex is evident from the different frontier orbitals of the different isomers, which can be directly seen in the corresponding STM images (*6*). Frontier orbitals have previously been imaged for the case of pentacene alone. We complement our results by using density functional theory (DFT) calculations.

The experiments were carried out with a home-built low-temperature STM operated at 5 K. NaCl was evaporated thermally onto clean Cu(111) and Cu(100) single-crystal samples at room temperature so that defect-free, (100)-terminated NaCl islands of two atomic layers in thickness were formed (*7*). Individual pentacene molecules and gold atoms were adsorbed at a sample temperature of $T \sim 5$ K, with the sample located in the STM. Bias voltages refer to the sample voltage with respect to the tip. All experimental data refer to the NaCl/Cu(100) system, except where stated otherwise.

Single-molecule chemistry by means of STM on an insulating surface follows a different route compared with the well-established manipulations on metal substrates, on which a single-
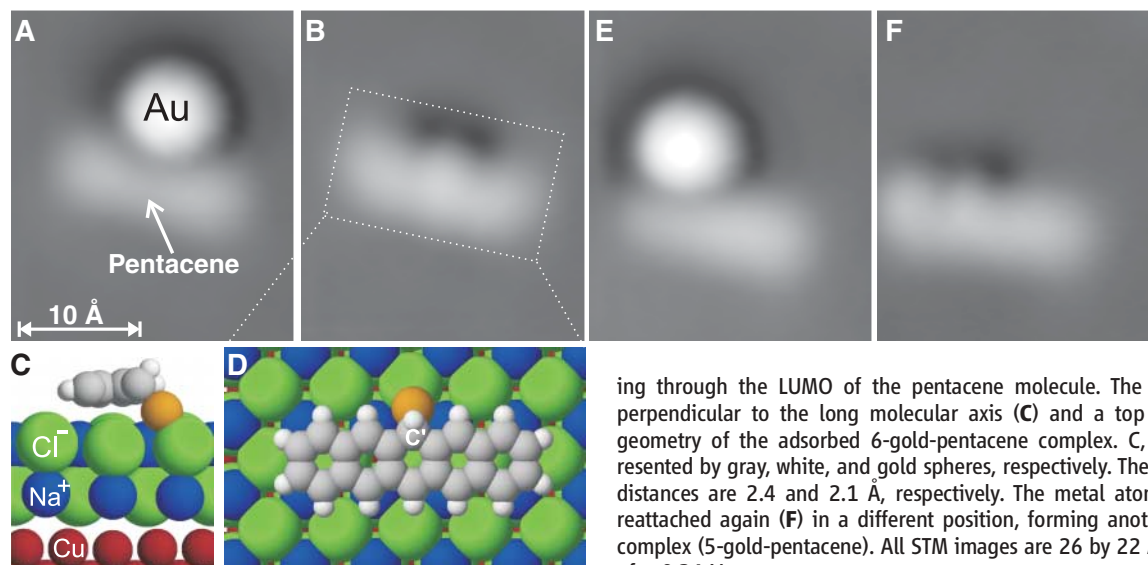

Fig. 1. Making and breaking a chemical bond between a single pentacene molecule and gold atom on an NaCl bilayer supported by a Cu(100) substrate. (**A**) STM image showing the molecule and the gold atom before bond formation. (**B**) Image showing a molecule-metal complex (6-gold-pentacene) after resonant tunneling through the LUMO of the pentacene molecule. The sphere models show a cut perpendicular to the long molecular axis (**C**) and a top view (**D**) of the calculated geometry of the adsorbed 6-gold-pentacene complex. C, H, and Au atoms are represented by gray, white, and gold spheres, respectively. The Au-Cl and Au-C interatomic distances are 2.4 and 2.1 Å, respectively. The metal atom can be detached (**E**) and reattached again (**F**) in a different position, forming another structural isomer of the complex (5-gold-pentacene). All STM images are 26 by 22 Å in size and taken at a bias of +0.34 V.

Electronic Confinement and Coherence in Patterned Epitaxial Graphene

Claire Berger *et al.*
Science **312**, 1191 (2006);
DOI: 10.1126/science.1125925